energies

MDPI

Article

Wind Farm Wake: The 2016 Horns Rev Photo Case

Charlotte Bay Hasager [1,*], Nicolai Gayle Nygaard [2], Patrick J. H. Volker [1], Ioanna Karagali [1], Søren Juhl Andersen [1] and Jake Badger [1]

[1] Department of Wind Energy, Technical University of Denmark, Frederiksborgvej 399, 4000 Roskilde, Denmark; pvol@dtu.dk (P.J.H.V.); ioka@dtu.dk (I.K.); sjan@dtu.dk (S.J.A.); jaba@dtu.dk (J.B.)

[2] DONG Energy A/S, Kraftværksvej 53, 7000 Fredericia, Denmark; nicny@dongenergy.dk

* Correspondence: cbha@dtu.dk; Tel.: +45-2132-7328

Academic Editor: Frede Blaabjerg
Received: 22 December 2016; Accepted: 27 February 2017; Published: 7 March 2017

Abstract: Offshore wind farm wakes were observed and photographed in foggy conditions at Horns Rev 2 on 25 January 2016 at 12:45 UTC. These new images show highly contrasting conditions regarding the wind speed, turbulence intensity, atmospheric stability, weather conditions and wind farm wake development as compared to the Horns Rev 1 photographs from 12 February 2008. The paper examines the atmospheric conditions from satellite images, radiosondes, lidar and wind turbine data and compares the observations to results from atmospheric meso-scale modelling and large eddy simulation. Key findings are that a humid and warm air mass was advected from the southwest over cold sea and the dew-point temperature was such that cold-water advection fog formed in a shallow layer. The flow was stably stratified and the freestream wind speed was 13 m/s at hub height, which means that most turbines produced at or near rated power. The wind direction was southwesterly and long, narrow wakes persisted several rotor diameters downwind of the wind turbines. Eventually mixing of warm air from aloft dispersed the fog in the far wake region of the wind farm.

Keywords: wind farm wake; fog; wake modelling; meteorological conditions

1. Introduction

As wind turbines extract energy from the wind, they leave regions of lower speed air in their wakes. For offshore wind farms, wakes are responsible for the largest single loss of energy production. Considerable effort is therefore being put to the analysis and modelling of wake effects [1–9]. Normally, the wakes are invisible, discernible only through the reduced production of downstream turbines caught in the wakes. But in recent years, wakes have been visualized and put under quantitative scrutiny (both onshore and offshore) through the deployment of remote sensing methods such as lidars [10–12], radars [13] and synthetic aperture radar [14,15].

However, direct visual observation of wakes in a wind farm remains rare. For this reason, two photographs taken on 12 February 2008 at the Horns Rev 1 offshore wind farm have become quite renowned, to the point where they have become the quintessential illustration of wind farm wakes. Even though the Horns Rev 1 photographs do not provide quantitative information about the flow field in the wakes, they do offer a dramatic illustration of the wake expansion, and of the turbulent nature of the flow in the wakes. Analysis of the images and of the meteorological conditions at the time revealed that the atmosphere was convective and that the wakes were captured by the re-condensation of fog. This process was triggered by the lifting and cooling of warm super-saturated air from the lower part of the rotor area by the swirling motion of the air in the wakes themselves [16,17]. The wind speed was low, only marginally above the cut-in speed of the wind turbines.

In this paper we examine new photographs of wind farm wakes, this time taken at Horns Rev 2 on 25 January 2016 at 12.45 UTC. In contrast to the well-known picture from 2008 with unstable conditions at Horns Rev 1, the Horns Rev 2 photographs are of wakes under stable atmospheric conditions. Thus the Horns Rev 1 and Horns Rev 2 wake photographs provide a visual insight on wakes for a broad range of atmospheric conditions. Studies show that wakes in stably stratified atmospheric boundary layer [18,19] differ materially from wakes in neutral and unstable conditions [20–22]. From the wind farm wake analysis we are able to improve our understanding of the diverse physical processes in the atmosphere. It is important in regard to siting and planning of offshore wind farms [6]. The topic has high relevance due to the ambitious plans on adding much more offshore wind power capacity in EU-27 and other countries worldwide [23,24].

The description of the wind farm and presentation of the photos are presented in Section 2. The meteorological conditions observed from meteorological ground-based instruments and satellites, described in Section 3, are collected and combined (Section 4). Such measurements form the basis for interpreting the local weather prevailing at Horns Rev 2 on 25 January 2016. The synoptic weather conditions are characterized from radiosonde data and atmospheric mesoscale modelling using the Weather Research & Forecasting (WRF) model (Section 5). The wind farm production data, an engineering wake model and large eddy simulation (LES) outputs for the wind farm wake dynamics are used to interpret the wind farm wakes seen in the photos (Section 6). A discussion on the key findings is presented in Section 7 and the main conclusions are summarized in Section 8.

2. Horns Rev 2 Photographs

The Horns Rev 2 wind farm is located in the North Sea west of Jutland, Denmark, see Figure 1. The wind farm consists of 91 wind turbines with hub-height at 68 m above mean sea level. Horns Rev 2 entered full operation November 2009. The four photographs taken by Bel Air Aviation Denmark from the helicopter window are shown in Figure 2. In two of the photos annotation on the wind turbines is included. See Figure 3 for further information on the wind turbine positions.

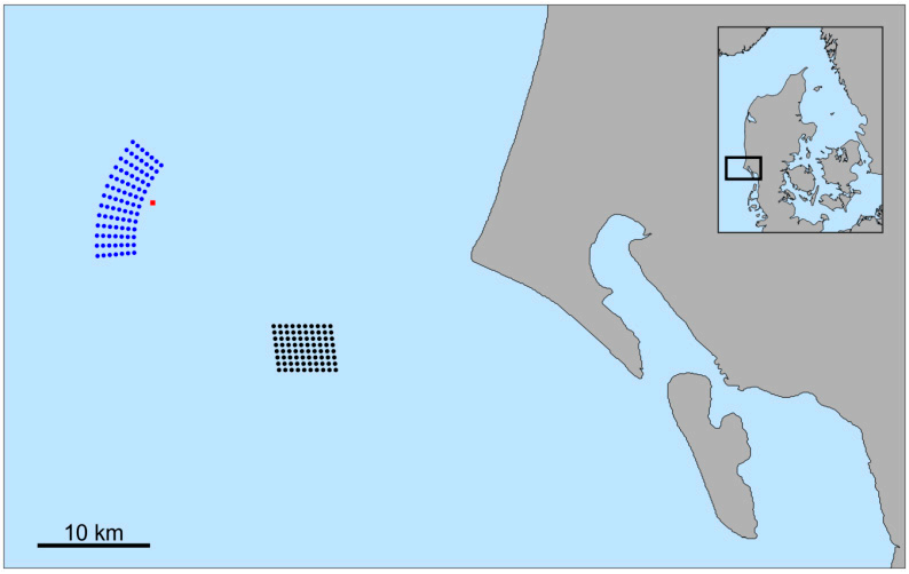

Figure 1. Location of Horns Rev 1 (black dots) and Horns Rev 2 (blue dots) wind farms in the Danish North Sea. The red square indicates the position of the transformer station.

(**a**)

(**b**)

Figure 2. *Cont*.

(**c**)

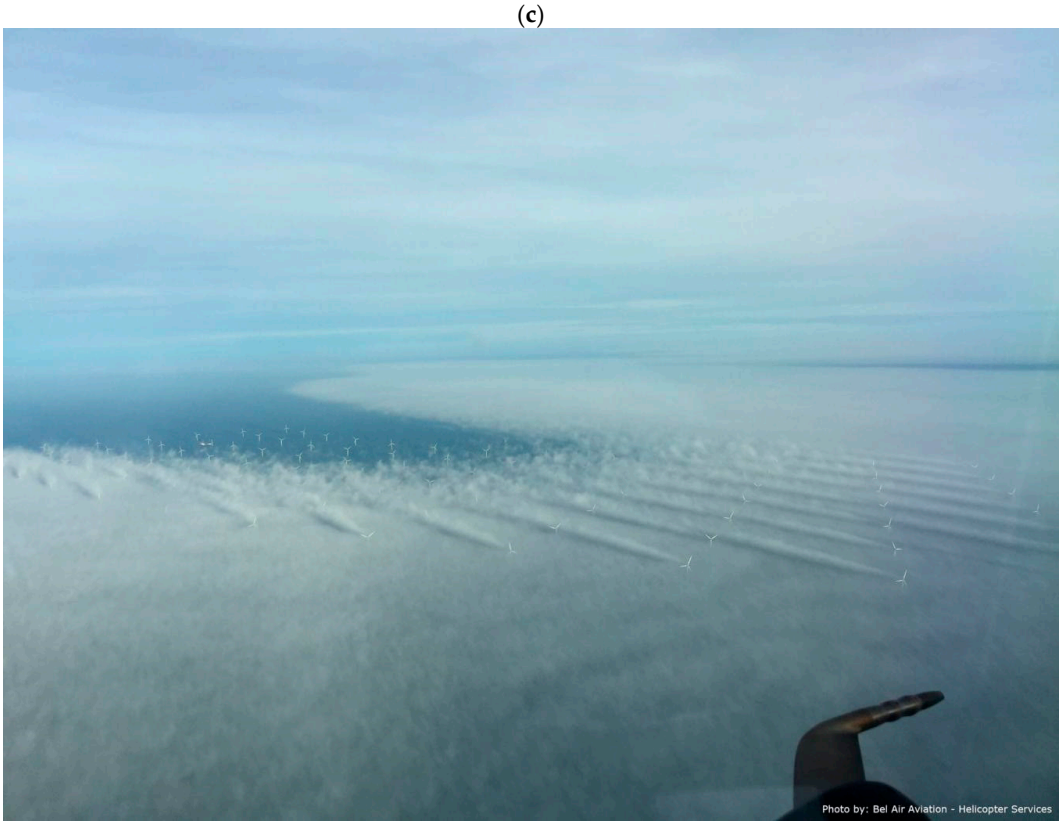

(**d**)

Figure 2. (**a**) Photograph of the Horns Rev 2 offshore wind farm on 25 January 2016 at 12:45 UTC seen from SSW direction; (**b**) Same as (**a**) but shortly after seen from SW; (**c**) Same as (**b**) but shortly after seen from WSW; (**d**) Same as (**c**) but seen from W on around 12:46 UTC.

3. Data Sources

3.1. Meteorological Data at the Wind Farm

The transformer station of Horns Rev 2 is located east of the wind farm and is equipped with a meteorological station providing air temperature, relative humidity and pressure measurements at 26 m above mean sea level. In addition, a WindCube v2 lidar situated on the deck of the transformer station observes wind speed and wind direction at ten vertical levels above mean sea level with the lowest at 65.75 m, and from 68.75 m to 245.75 m for every 20 m. The lidar is a commercially available pulsed lidar, which derives three-dimensional wind speed components from line of sight Doppler spectra of four infrared laser beams arranged on a cone with fixed elevation angle [25]. The wind speed uncertainty is less than 3% [26]. Local meteorological observations of wind speed, wind direction, vertical wind shear and veer, turbulence intensity, temperature and pressure are analyzed. The turbulence intensity is defined as the ratio between the standard deviation and the mean value of the wind speed over ten minutes. We note that turbulence intensity measured by a lidar is not as accurate and precise as turbulence data from a sonic anemometer [27]. However, we do anticipate that the turbulence intensity measured by the lidar, is indicative of the general turbulence level. Figure 3 shows the positions of the wind turbines and the transformer station (413,233 m Easting, 6,162,401 m Northing, UTM zone 32 N).

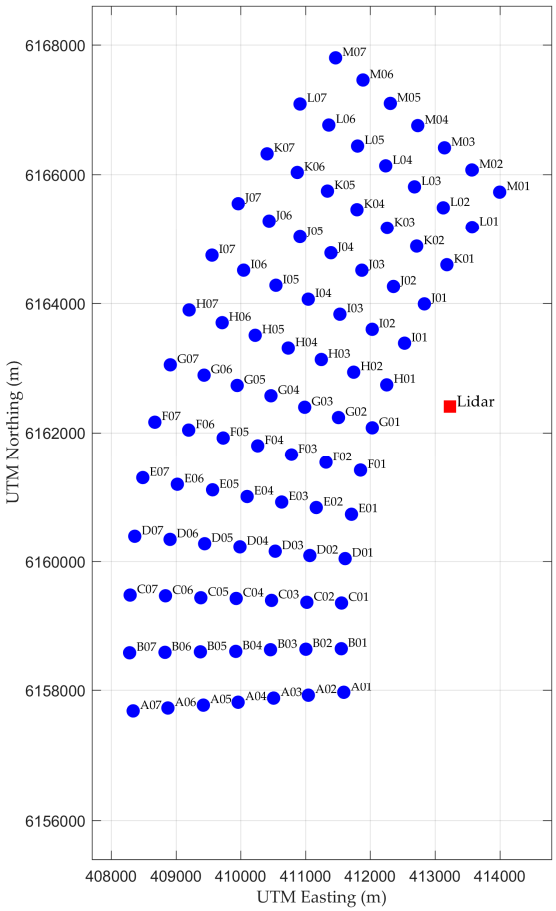

Figure 3. Layout of the wind farm and the transformer station (red square).

3.2. Satellite Data

The Advanced Scatterometer (ASCAT) on board the Metop-A & B platforms has been in orbit, retrieving wind speed and direction over the ocean, since 2006. Scatterometers are radars that transmit

microwave pulses towards the Earth's surface and measure the backscattered signal. Bragg scattering is the primary process in the case of water surfaces; the radar signal is scattered due to the small-scale ripples on the water surface, and a portion of the signal is backscattered to the instrument. These ripples are assumed to be in equilibrium with the wind stress and by measuring the radar backscatter, a wind speed and direction can be inferred. The Royal Netherlands Meteorological Institute (KNMI) produces the coastal ASCAT scatterometer product within the framework of the European Organization for the Exploitation of Meteorological Satellites (EUMETSAT) Ocean and Sea Ice Satellite Application Facility [28]. This product includes retrievals of wind speed and direction (equivalent neutral wind at 10 m) within a wind vector cell of size 12.5 km by 12.5 km.

Sea surface temperature (SST) is routinely observed from space with the use of microwave and infra-red sensors. Microwave instruments have the advantage of retrieving SST independent of cloud coverage. Their spatial resolution is coarse and the measurement depth is that of the sub-skin (mm). Infrared sensors such as the Spinning Enhanced Visible and Infrared Imager (SEVIRI) cannot retrieve SST when overcast, but they have a high spatial resolution and the measurements are of the skin (1 μm). SST retrievals from different sensors are blended in a daily gap-filled level-4 SST analysis [29], produced by the Danish Meteorological Institute (DMI) according to the GHRSST (Group for High Resolution SST) product specifications. The regional multi-sensor SST climate data record used in this study was developed with consideration of the regional conditions that apply to the North Sea and Baltic Sea [30].

4. Data Presentation

Ocean surface winds at 10 m are observed from ASCAT at 10:26 UTC and 21:03 UTC. The wind field for the morning retrieval is shown in Figure 4a. The general wind direction is from the southwest. The wind speed is lower near the coast, in particular in the northern part of the region, than further offshore. Near the Horns Rev 2 wind farm the wind direction is 217° and the wind speed is 7.8 m/s in the morning pass. In the evening retrieval, the wind direction is 214° and the wind speed is 10.9 m/s.

The sea surface temperature in the region observed from the regional multi-sensor SST climate data record from DMI is shown in Figure 4b. A strong horizontal gradient in temperature ranging from 7 °C in the west to below 3 °C near the coast of Jutland is noticed. In the vicinity of the Horns Rev 2 wind farm the temperature is 5.2 °C. Hourly satellite SST retrievals from SEVIRI are not available some hours prior to and during the time of the obtained photos. This indirectly verifies that it was overcast. In such conditions no warming of the sea surface is to be expected [31,32].

Time-series of lidar measurements on wind speed and direction at hub height from Horns Rev 2 are shown in Figure 5; the instantaneous 10-m ASCAT wind retrievals are also presented for reference.

For a large fraction of the day in question, the wind direction is such that the lidar is in the wake of the wind farm. Consequently, we need another reference to estimate the freestream wind speed. We use the ten-minute mean wind speed recorded by the turbine nacelle anemometers. This is retrieved from the wind farm Supervisory Control and Data Acquisition system (SCADA). For southwestern winds turbine A07 would be a good candidate for measuring the undisturbed inflow. However, at the time of the photographs this turbine was stopped for maintenance. Instead, we use its neighbors A06 and B07, taking the maximum nacelle anemometer wind speed between the two as the proxy for the freestream wind speed, also shown in Figure 5. The freestream wind speed is generally above the wind speed measured by the lidar, as expected when the lidar is in the wake.

Similarly, for those wind directions, the turbulence intensity is elevated at the lidar location at hub-height, as evidenced by Figure 6. This is a consequence of the increased turbulence in the wind turbine wakes, which sweep over the lidar for most of the day, with the exception of the late afternoon/early evening. The ambient turbulence intensity ranges from 3% to 5% in un-waked conditions, while during waked conditions at the time of the photos the turbulence intensity is ~8%. We illustrate this in Figure 6 by calculating the wind directions, where the lidar is in the wake of at

least one wind turbine. We use the Park wake model [33] with a linear wake expansion parameter of 0.04, which is appropriate for offshore sites [6].

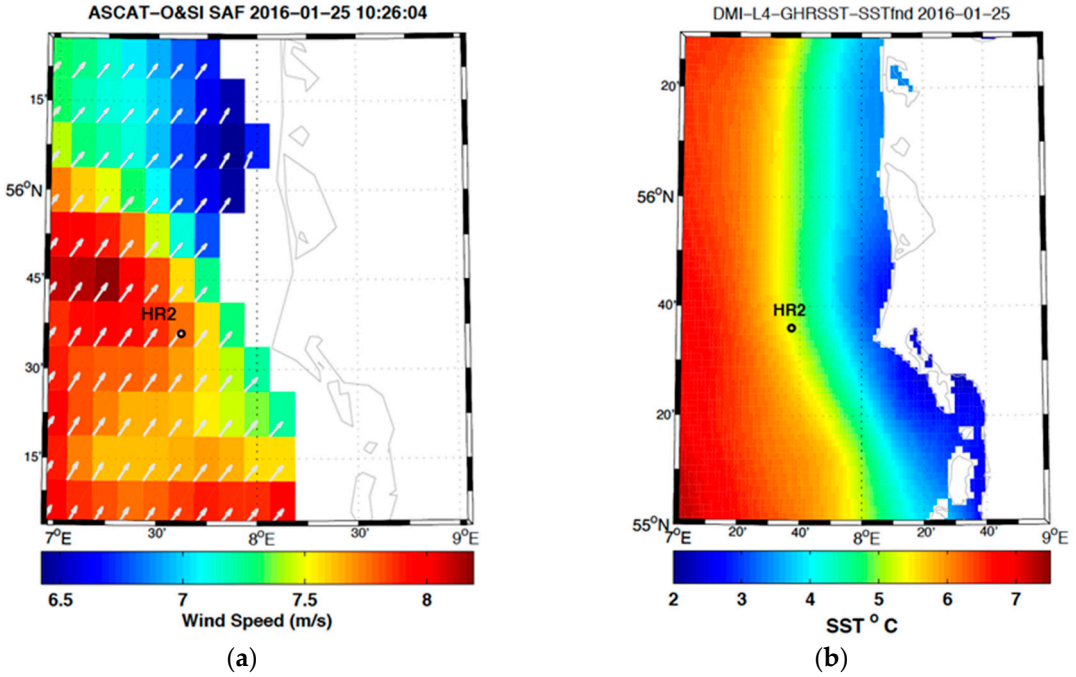

Figure 4. Maps covering the southeast North Sea near Horns Rev 2 (HR2): (**a**) Wind speed and direction observed on 25 January 2016 at 10:26 UTC by ASCAT from KNMI; (**b**) Sea surface temperature daily average on 25 January 2016 from DMI.

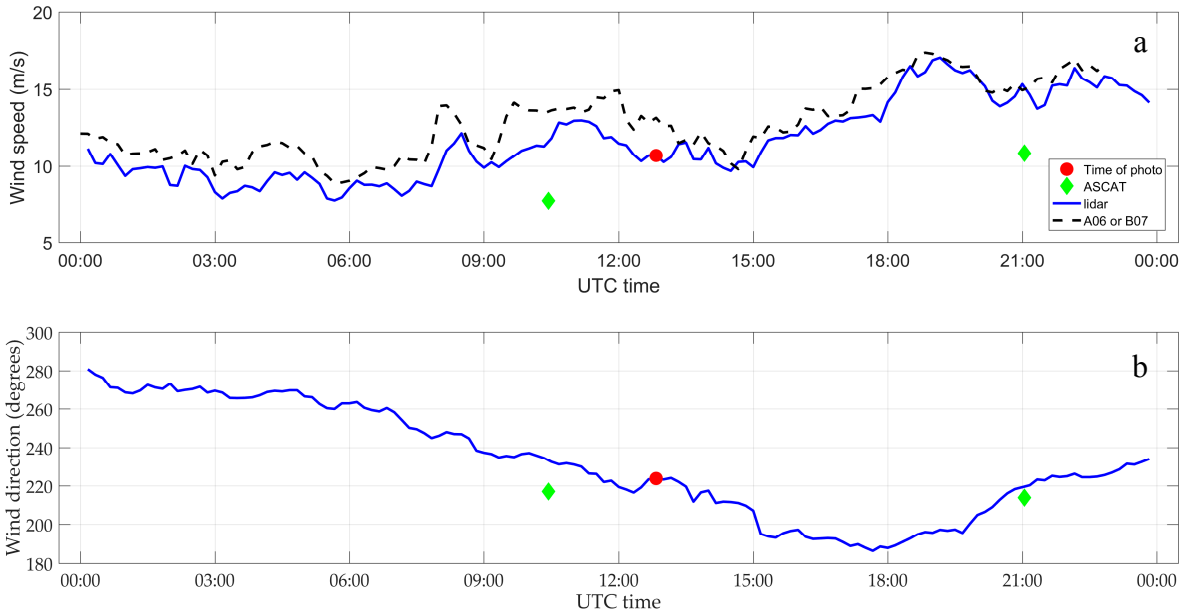

Figure 5. Time series of (**a**) wind speed and (**b**) wind direction on 25 January 2016 observed at hub height. The red dot indicates the time of the photos and the green diamonds are the ASCAT observations at 10 m. In the top panel, the dashed black line is the freestream wind speed estimated from wind farm SCADA data.

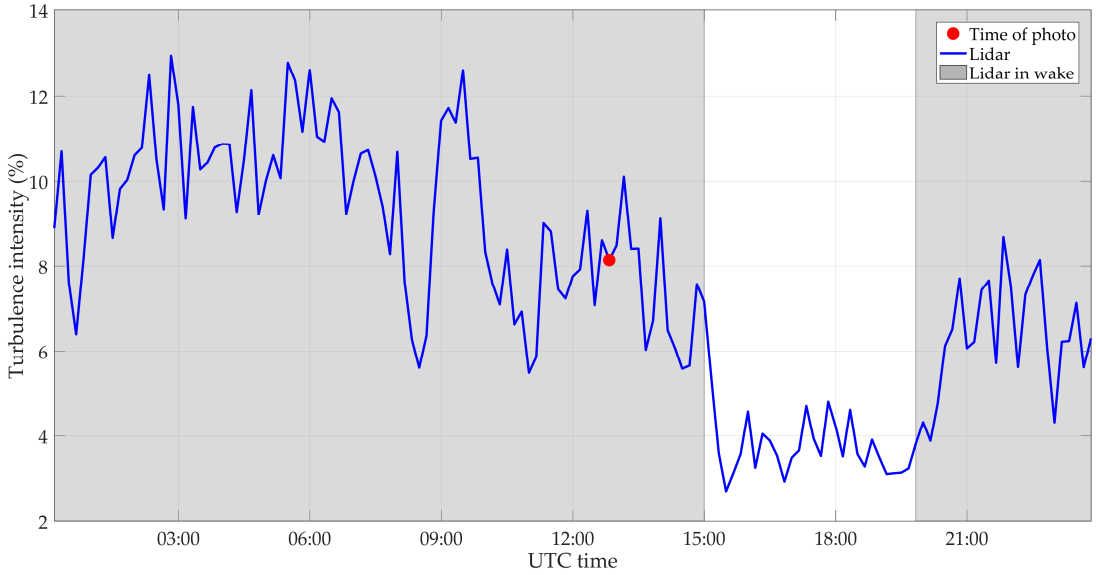

Figure 6. Time series of the lidar turbulence intensity at hub height on 25 January 2016. The red dot indicates the time of the photographs. The grey regions correspond to times, where the wind direction is such that the lidar is in the wake of the wind farm (see text).

Air temperatures (observed at 26 m at the transformer platform) decrease from around 10 °C to 6 °C between 9:00 and late afternoon. The pressure drops linearly from 1016 hPa to 1008 hPa on 25 January 2016 between 9:00 and 24:00 UTC as shown in Figure 7. The virtual potential temperature, calculated from the air temperature, pressure and the relative humidity, shows a similar variation. The satellite-based SST value of 5.2 °C shows a colder surface than the air mass above. From the combined information of satellite-based SST and air temperatures it is found that the atmospheric stratification is stable.

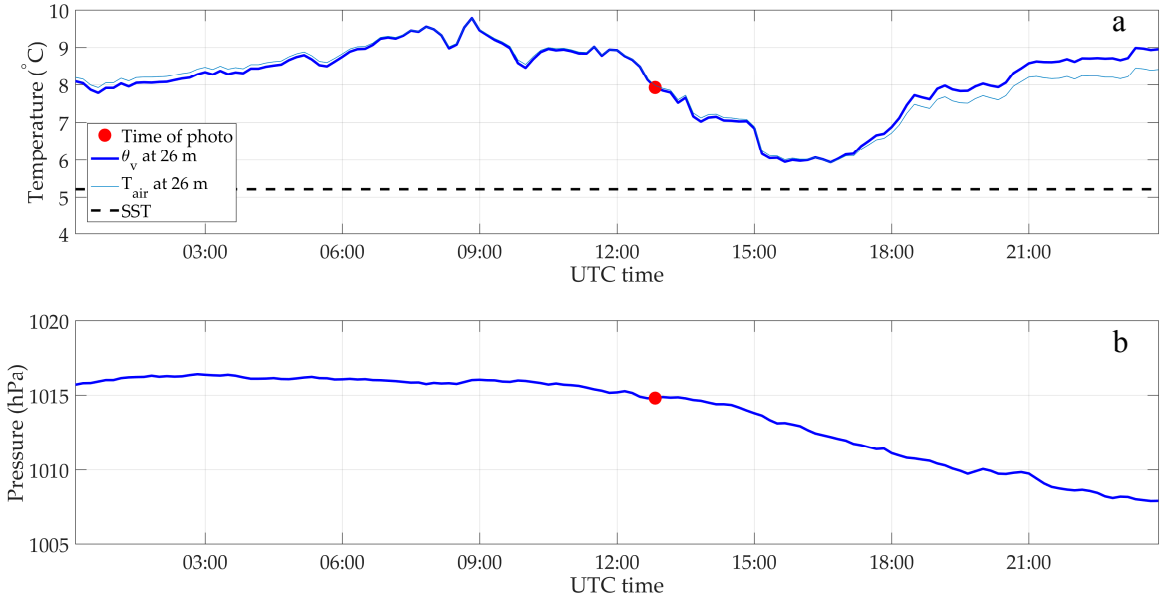

Figure 7. Time series of (**a**) virtual potential temperature (θ_v) and absolute temperature (T_{air}) and the dashed line shows sea surface temperature from satellites and (**b**) pressure (bottom panel) on 25 January 2016. The red dot indicates the time of the photographs.

The atmospheric conditions in the vertical dimension at and around the time of the photos are further investigated. The vertical variability in horizontal wind speed (wind shear), wind direction (wind veer) and turbulence intensity observed from the lidar at the time of the photos is shown in Figure 8. The lidar data are listed in Appendix A Table A1 and meteorological data in Table A2. The lidar data show a wind speed increase with height, wind turning clockwise with height while the turbulence intensity decreases with height. It can be noted that the wind turbine hub-height is 68 m and the rotor diameter is 93 m; thus, blade tips extend from 21.5 m to 114.5 m above mean sea level. The data characterize the atmospheric boundary layer from hub-height to around 200 m above mean sea level.

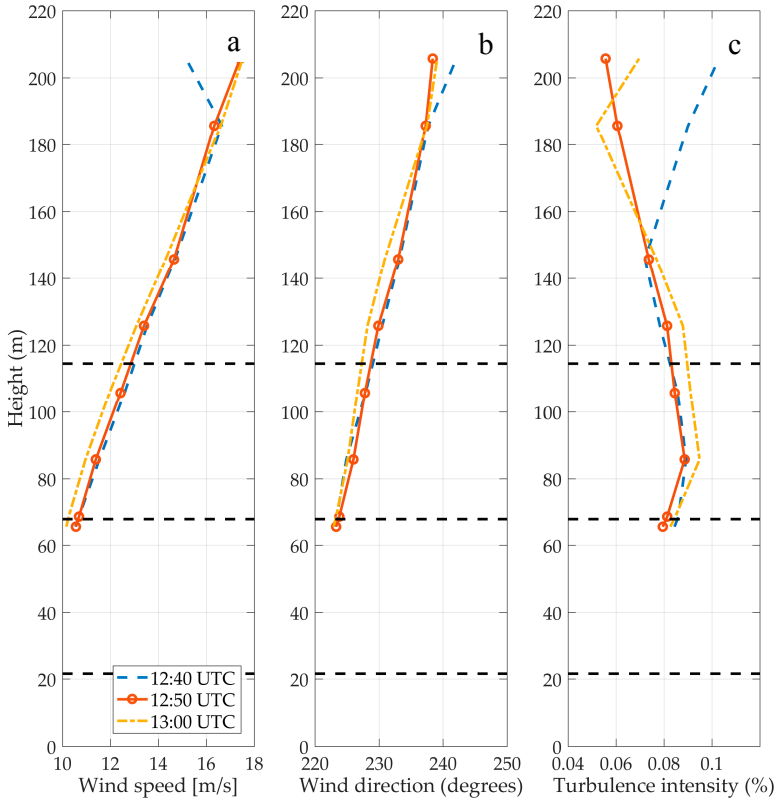

Figure 8. Lidar observations at Horns Rev 2 on 25 January 2016 from 10-min averages at 12:40, 12:50 and 13:00 shown as function of height for (**a**) mean wind speed; (**b**) wind direction and (**c**) turbulence intensity. Hub height and upper/lower tip heights are indicated by the black dashed lines.

5. Weather Conditions and Meso-Scale Modelling

The synoptic weather conditions are interpreted based on satellite cloud cover observations, weather forecast, radiosonde data and WRF model results. Several satellites observed the cloud cover over the region in the late morning on 25 January 2016. Figure 9 shows a combined cloud cover product, from ECMWF [34], at 13:00 UTC. Horns Rev is overcast, as also visible in the photos (Figure 2c,d). As interpreted from the ECMWF weather forecast [35], there was a passage of a warm front. A warm air mass was advected from the southwest, associated with a high pressure over central Europe and a low pressure over eastern north Atlantic. Radiosonde data are available at Norderney [36]; an island in the Wadden Sea around 200 km SSW of Horns Rev. The radiosonde data show strong veering (not presented) in the lowest 3 km, indicative of strong warm advection, consistent with the warm front. The veering is consistent with the observed change in wind direction at the wind farm (Figure 8). The cloud cover at Norderney is similar to that at Horns Rev (Figure 9).

For the numerical weather prediction simulations we use the WRF model [37]. WRF has ability to model a stable stratified marine boundary layer according to [38]. The model domain

is shown in Figure 10. The outer and lower boundaries are forced by ERA-Interim [39] and the SST is from DMI's high resolution data [29]. For the surface layer description, we used the Mellor-Yamada-Nakanishi-Niino (MYNN) surface layer scheme that applies Monin-Obukhov similarity theory [40]. Nudging only takes place in the outer domain. In the vertical direction, we defined in total 70 vertical levels, 23 of which are in the first 500 m. For the turbulence mixing in the vertical direction, we used the MYNN 2.5 planetary boundary layer scheme [41]. Then, the innermost domain is run twice, once without and once with the Horns Rev 1 and 2 wind farms. The wind farms are parametrized by the Explicit Wake Parametrisation (EWP) [42]. A 36-h spin-up period prior to 25 January 2016 at 13:00 UTC, i.e., 15 min after the photos are taken, is applied.

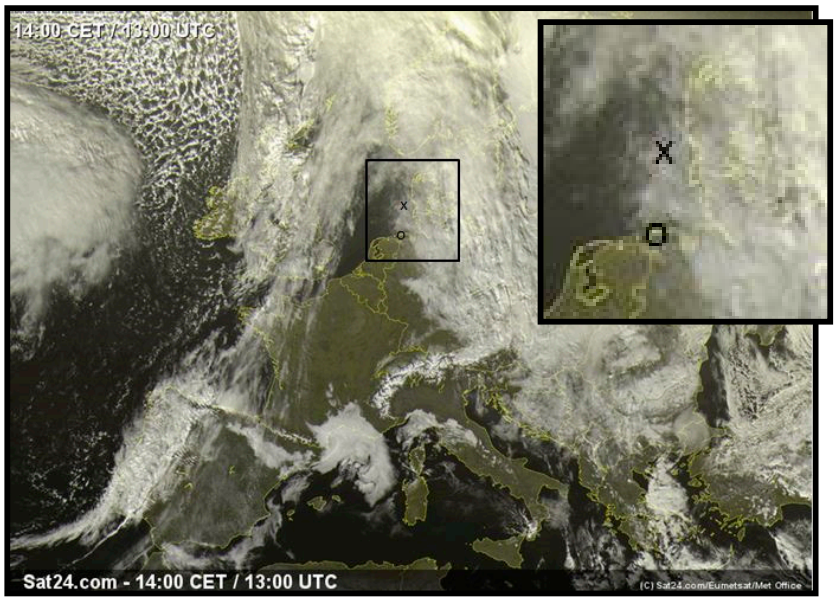

Figure 9. Cloud cover from ECMWF [34] on 25 January 2016 at 13:00 UTC for Europe. Horns Rev and Norderney are indicated by x and o, respectively. Zoomed-in area is inserted.

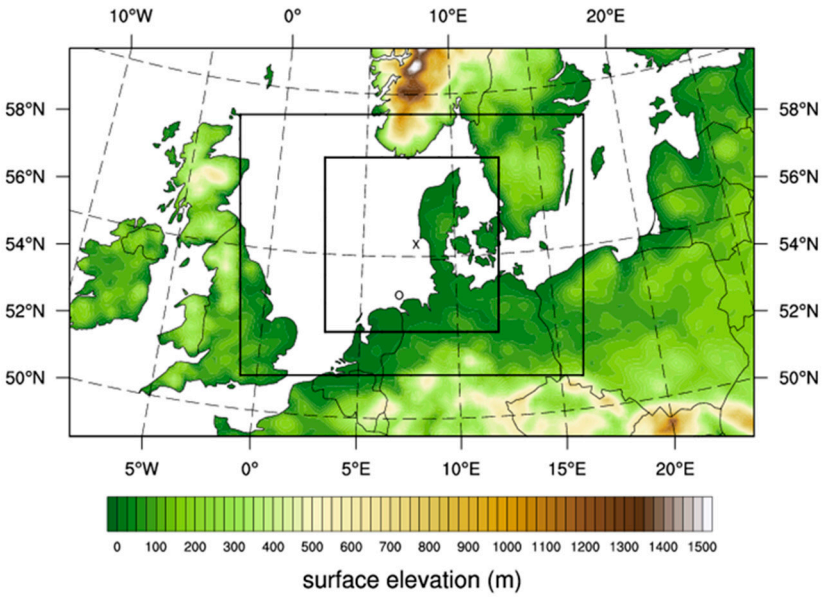

Figure 10. WRF domain for which the outer domain has a grid size of 18 km by 18 km, the inner domain has grid size 6 km by 6 km and the innermost domain has a grid size of 2 km by 2 km. Horns Rev and Norderney are indicated by x and o, respectively.

The WRF model results compare well with radiosonde data on temperature and relative humidity (Figure 11).

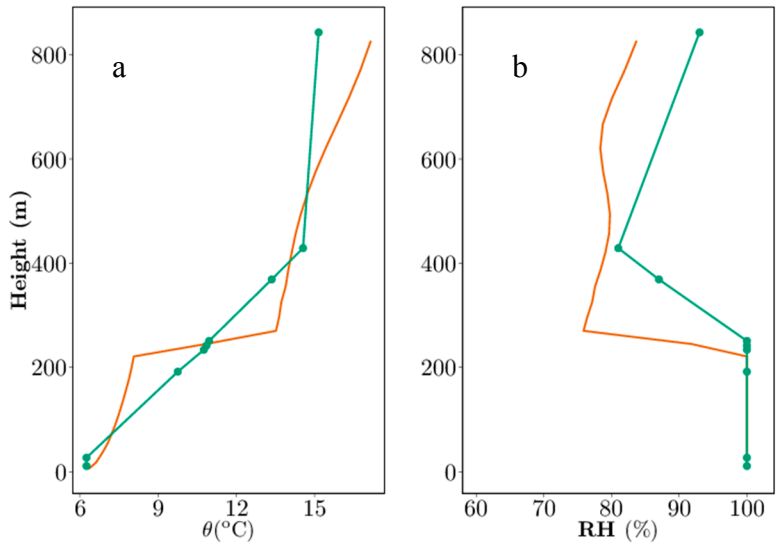

Figure 11. Observations from Norderney radiosonde [36] (green) and WRF model results (red) shown on 25 January 2016 at 12:00 UTC (**a**) potential temperature (Θ) and (**b**) relative humidity (RH).

The modelled boundary layer height is around 240 m at the inversion. The radiosonde measurements at Norderney show a 400 m thick temperature inversion directly above the cold sea surface. The modelled temperature gradients in the first 400 m are similar. However, the temperature stratification is slightly different in the model. Instead of an inversion layer with a constant temperature lapse rate, it simulates a mixed layer in the first 200 m, which is capped by a steep inversion.

WRF results include vertical profiles from 0 to 600 m of wind speed, turbulent kinetic energy (TKE), temperature and liquid water content. The results at Horns Rev are presented in Figure 12 for calculations without and with the wind farms included in WRF. The profiles present an average over the Horns Rev 2 wind farm. As expected, compared to the freestream wind speed conditions from the simulations without the wind farm, the wind speed reduces when the wind farm is included. The TKE increases above hub-height and decreases below hub-height, due to an increased and decreased TKE shear production, respectively. The temperature profile—a mixed layer capped by a strong inversion—looks very similar to that at Norderney. The simulations show liquid water content of around 0.1 g/kg at hub-height.

The difference in liquid water content between the simulation without and with wind farms in the horizontal plane at hub-height is shown in Figure 13. We find reduced liquid water content of up-to around 0.03 g/kg in the wake of the wind farm that extends in the North-East direction, which is caused by the mixing in of warm air from aloft. This reduction of the liquid water content corresponds to the tendency in dissolving the fog layer at the end of and behind the Horns Rev 2 wind farm in the photos.

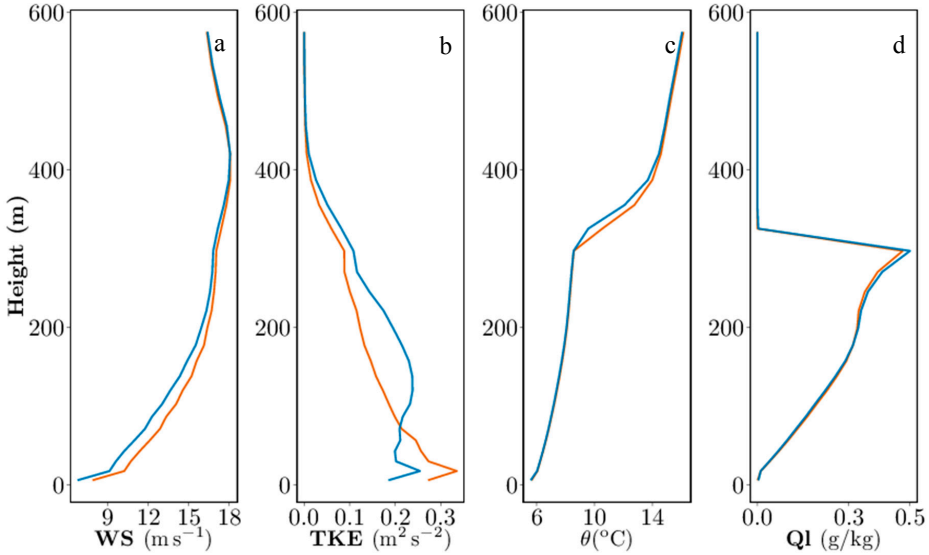

Figure 12. WRF model results at Horns Rev show the wind farm averaged atmosphere without wind farm (red) and with wind farm (blue) for (**a**) wind speed (WS); (**b**) turbulent kinetic energy (TKE); (**c**) temperature (θ) and (**d**) liquid water content (Q_l).

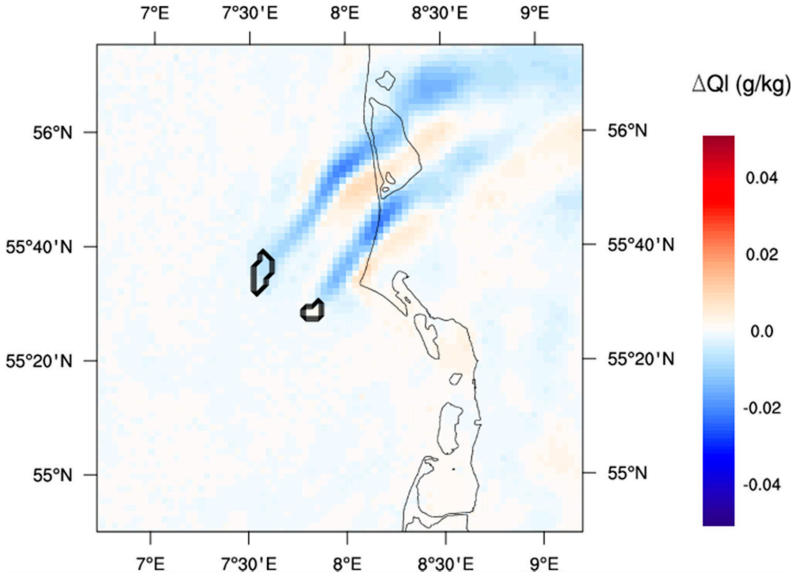

Figure 13. WRF model result at Horns Rev showing the difference in liquid water content (ΔQ_l) at hub-height between simulations with and without wind farms. The blue shading shows dryer conditions downstream of the wind farms.

6. Wind Farm Data and Wake Modelling

6.1. SCADA Data and Park Wake Model

Figure 14 gives an overview of the flow conditions through the wind farm at the time of the photographs by means of the Horns Rev 2 SCADA data at each turbine position. Specifically, the wind speed from the nacelle anemometers are indicated by the length of the arrows and by the color scale. The wind direction based on the yaw direction sensor is compared to the wind direction observed at the lidar. The yaw direction signals of the wind turbines have been individually calibrated by removing any mean offset between the yaw direction and the lidar wind direction for the month of

January 2016. Both wind speed and wind direction vary across the wind farm. In the northeastern part of the wind farm wind directions are similar to lidar measurement while deviations are up to 7° in the southern row of turbines. SCADA data are listed in Appendix A Table A3. Three turbines (A07, G07, and L03) were stopped for service or idling at the time of the photographs. For two additional turbines (H07 and J04) no SCADA data were available at this time, but both were running normally. The turbines with missing SCADA data are marked with question marks in Figures 14 and 15.

The power production from SCADA data and the Park wake model result at the time of the photos are shown in Figure 15. The production is near rated power at most turbines. Production lower than 1900 kW at few turbines clustered in the southeastern area is noted. The model result presented in Figure 15 is based on 91 Park model simulations, one for every turbine. The Park model simulations all have the same inflow wind speed. This is defined as the mean wind speed among the turbines in the front row. But in each Park model calculation the inflow wind direction is set to the local wind direction at a given wind turbine (from Figure 14). The output of a particular calculation is the predicted power of a single turbine. Thus this method takes the variation of the inflow wind direction into account in a crude way, since it fails to account for the effect of a wind direction gradient on the upstream wakes. But it does improve the agreement with the SCADA wind power production data for a single timestamp. The root mean square error normalized to the mean power produced by the turbines at this instance changes from 16% (using the lidar wind direction as the inflow direction in a single simulation) to 7% (91 simulations using the local wind direction for the model input). However, when averaging over one or multiple years of wind farm production the effect of wind direction gradients is greatly diminished.

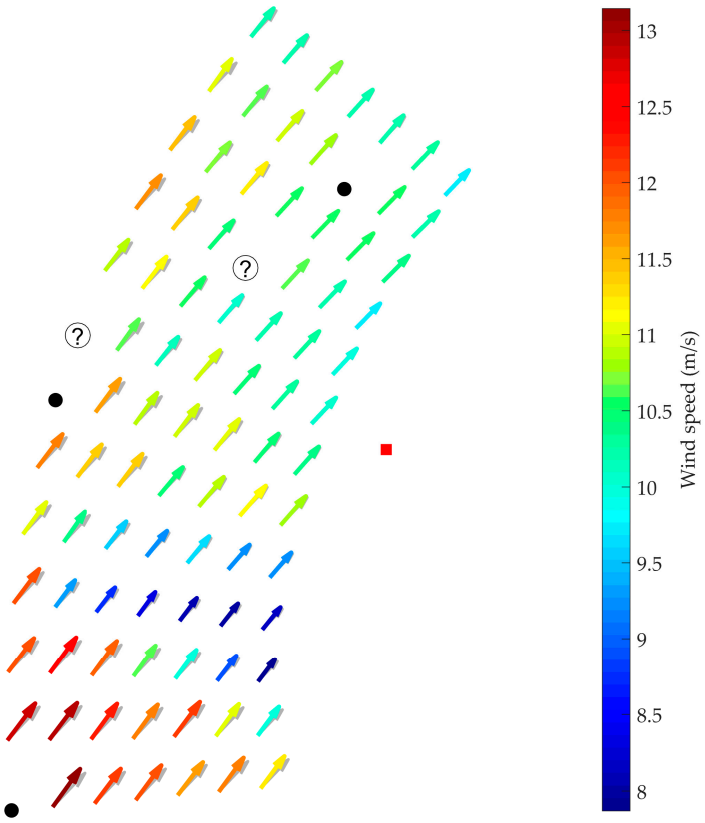

Figure 14. Horns Rev 2 wind speed from nacelle anemometers (length of arrows and in color scale) and wind direction (direction of arrows) from the yaw direction sensor at each turbine position on 25 January 2016 at 12:50 UTC and in grey arrows same wind speed as at nacelles but wind direction measured by the lidar located on the transformer platform (red square). Black dots indicate stopped wind turbines. Circles with question marks represent wind turbines operating normally but with no available SCADA data.

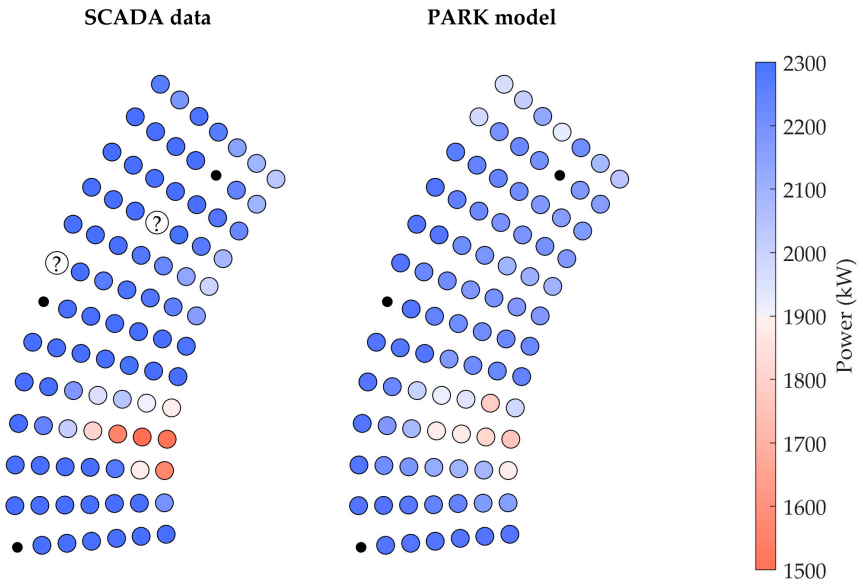

Figure 15. Horns Rev 2 wind turbine power production on 25 January 2016 at 13:00 UTC observed with SCADA and modelled by the Park wake model. Black dots indicate stopped wind turbines. Circles with question marks represent wind turbines operating normally but with no available SCADA data.

Thus the wind direction input to the Park model is important in this case due to the low wake expansion, most turbines being in part wake conditions, and only few in full wake. Figure 16 shows the Park model wake velocity deficit result of a single simulation with input of wind speed as average of the front row turbines and wind direction from the lidar. The turbines with lowest production are in full wake while most other turbines appear to be in partial wake regions. The photos in Figure 2 also show most turbines to be in partial wake and few in full wake.

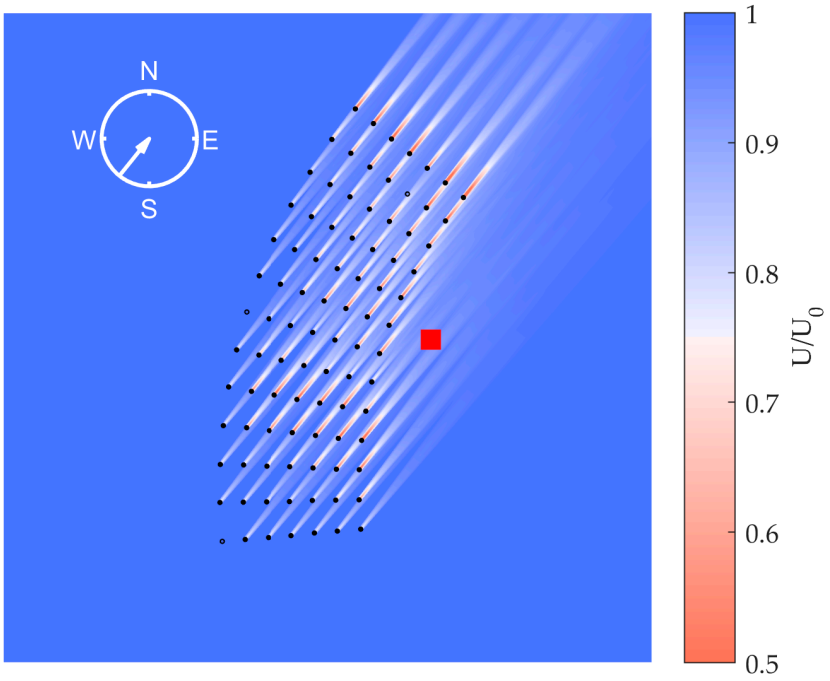

Figure 16. Horns Rev 2 wind farm wake from the Park wake model as velocity deficit. The red square indicates the transformer platform.

6.2. Large Eddy Simulation (LES)

A single turbine is modeled numerically using LES to elucidate the wake mixing. The simulation is performed using EllipSys3D, an incompressible Navier–Stokes solver [43,44]. The turbine is modeled using the actuator line method to represent the turbine and LES to get time resolved turbulent flow. Turbulent fluctuations derived from the Mann model [45], as well as the vertical shear and veer are modeled by explicitly imposing body forces into the flow. Hence, the inflow profile is derived and imposed directly from Figure 8. The turbine hub height is 1.46R (R is rotor radius) and the simulation is run for approximately 400 s. An overview of the employed methodology is given in [46].

The flow is visualized by continuously seeding particles every 1.6 s immediately upstream of the turbine, and translating them downstream as passive tracers according to the local velocities. Figure 17 shows instantaneous particle positions, only particles within the wake are shown for clarity. The blue particles were initially released between Z = [0–0.46]R, i.e., below the turbine, while the green particles were released between Z = [0.46–0.96]R, i.e., from bottom tip and half a turbine radius up. Figure 18 shows the particles located at sections at X = 3–5R, 7–9R, and 11–13R behind the turbine. Clearly, a substantial amount of particles is lifted into the wake by the turbine rotation and turbulent fluctuations. The turbine has clockwise rotation, thus the wake rotates counter-clockwise. Hence, the particles are concentrated in the lower and left side of the wake as seen from behind.

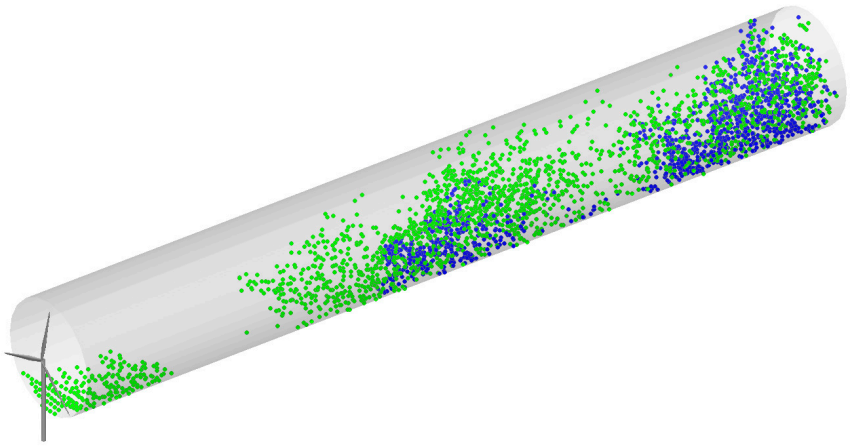

Figure 17. Visualization of wake development. Blue particles were initially released from Z = [0–0.46]R and green from Z = [0.46–0.96]R.

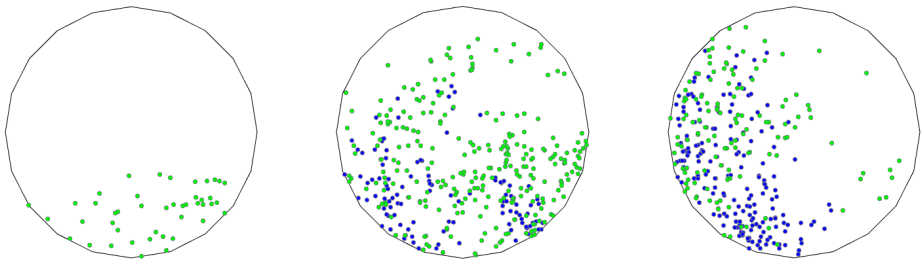

Figure 18. Particles located at sections at X = 3–5R, 7–9R, and 11–13R behind the turbine. Seen from behind.

The LES framework is not solved for the temperature, but the particles are assumed to act as a very crude proxy for the air mixture by assigning an initial temperature and mixing ratio to each of the particles. The pressure profile is assumed to be in hydrostatic equilibrium and the temperature profile was assumed to be the same as at Norderney. The air is assumed to be condensed below the rotor (Z = 0.46R) and nearly saturated (relative humidity of 98%) across and above the rotor

(Z > 0.46R). The Clausius-Clapeyron relation for the saturation vapor pressure is used to derive the initial mixing ratio. The particles are crudely assumed to maintain their initial temperature and mixing ratio along their entire trajectory. The relative humidity is examined for each time-step by computing an average temperature and mixing ratio based on the local particles within volumes of approximately 24 m $\times$ 24 m $\times$ 12 m, corresponding to a grid 12 $\times$ 12 $\times$ 6 times coarser than the flow field in the x, y, and z direction. On average, each average temperature and mixing ratio was based on approximately 15 particles. A threshold of 99.9% was used on the average relative humidity to determine if a given volume tends to condense or not. The contours of average condensation is plotted for five different height intervals in Figure 19 in blue (no-condensed) and white (condensed), where the turbine is marked in black and the 90% contour of the freestream velocity at the specific height is shown in red to highlight the wake. Despite the crude assumptions, Figure 19 clearly shows how the air tends to condense in the wake behind the turbine and furthermore the condensation tends to cover more in the lower parts of the wake, i.e., on the left side of the wake looking upstream corresponding to the areas where particles are predominantly lifted by the wake rotation. The analysis does not include the advection of already condensed volumes, but Figure 19 could indicate that condensation occurs in the near wake, before being advected downstream.

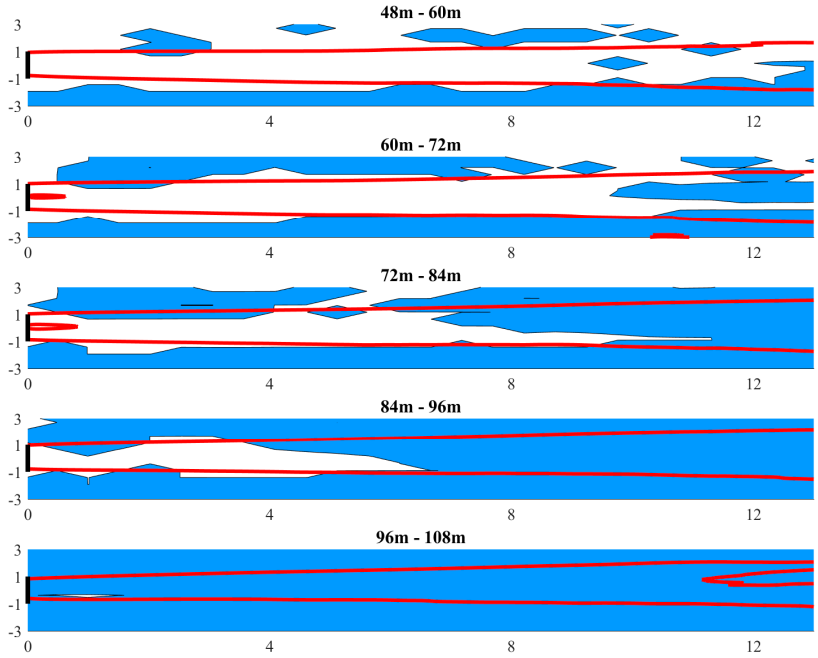

Figure 19. Average condensation contours shown in white for a threshold of 99.9% and no-condensed areas in blue for five different height intervals. The rotor (black lines) and the 90% freestream velocity contour for a given height (red). Note, that the freestream velocity changes with height. The wake is seen from above.

7. Discussion

The photos taken on 25 January 2016 at 12:45 UTC demonstrate that wind turbines influence the atmosphere. Upwind of the wind farm at the front row of turbines the fog layer is less than 20 m deep. The undisturbed fog is located below the lower tip of blades. This shallow fog layer is cold water advection fog of maritime origin [47]. The warm saturated air mass was advected from the southwest, where the SST was higher than at Horns Rev. A strong gradient in SST in the region with colder water near the coast enhanced the favorable conditions for the generation of cold water advection fog. The air temperature at Horns Rev is around 8 °C and the sea around 5 °C, thus stable atmospheric

stratification prevail, with a shallow layer of fog above the ocean surface; this resulted in this new wake visualization case.

For stable conditions strong clockwise wind veering is expected in the surface layer [48]. The waked lidar data from hub height to 200 m shows around 17° veering. The wind direction observed at 10 m from ASCAT is consistent with around 5° veering compared to lidar hub height data. Also the Norderney radiosonde data confirms strong veering.

For stable conditions strong shear is expected in the surface layer [49]. At the waked lidar position the wind speed at hub height is 11 m/s and at 200 m 18 m/s, while the freestream wind speed at the front turbines is 13 m/s. Satellite data at 10 m height shows around 2 m/s lower wind speeds than the lidar data. The satellite wind speeds are representative at 10 m above the surface, assuming neutral atmospheric stratification. The atmospheric stratification in this case is stable, thus, an underestimation of the 10 m wind speed is to be expected. Yet the combined picture of local winds at Horns Rev confirms strong wind shear. The ambient turbulence intensity is low (~3%) also indicative of stable conditions.

In general, there is an overall agreement of evidence between the synoptic weather conditions, the satellite observations, the in situ observations and the WRF model outputs. This agreement leads to a confidence in having provided a consistent description of the conditions under which these new, spectacular images of wind turbine wakes emerged.

The turbines in the front row produce at rated power (2300 kW) as the freestream wind is at rated speed (~13 m/s). The wind direction is such that only few downstream turbines are in full wake. Interestingly, the wind direction is not homogenous over the wind farm according to the SCADA data. In the southern row of turbines the wind directions vary. It is found that the Park wake model provides better agreement to power production data using multiple simulations of inflow wind direction than one simulation. Thus the general assumption of homogenous, stationary flow for the entire wind farm is not fulfilled as required by the wake model [33], and a piecewise model effort therefore is necessary in this case.

During stable conditions long, narrow wind wakes are to be expected [18,19]. From inspection of the photos the fog cones downstream of the front row of turbines are slightly larger than one rotor diameter at a distance of several rotor diameters downwind. The separation distance between turbines C07 and D06 is 11.4 rotor diameters (1058 m), and the direction between these turbines is 216°. Due to the curved wind farm layout different distances are found between turbines. The question though is to which degree the fog cones and the wind turbine wakes are related. Model results from LES, including a temperature scheme, indicated condensation in the near wake. It is found that warm near-saturated air above a colder sea is condensed to fog in the near wake. This occurs when the dew-point temperature is reached primarily in the lower part and in the left side of the wake, when seen from behind. The LES results provide a novel and good comparison to the visually observed fog cones of the full scale wind turbine wakes.

Clearing of the fog is noticed in the far wind farm wake region in the photos. The ocean is visible as well as several turbines and a service ship (near turbine L03). The WRF model results on liquid water content at hub-height, without and with the wind farm, show a tendency in dissolving the fog layer downstream of the wind farms (Figure 13). The process is caused by mixing of warm air from aloft to the surface. The horizontal extend of the clearing of fog in the photos is hard to outline but seems to last very long. The results from WRF show drying effects due to the wind farms more than 100 km downwind and also persist over land, in Jutland.

Previous studies [3,50,51] have documented that large wind farms on land impact the atmospheric conditions such that increased land surface temperatures (LST) are observed in stable stratification, typically during nighttime. This has been explained from downward mixing of warm air from aloft. Similar results for offshore wind farms have not been published (to our knowledge). Yet stable conditions occur offshore. According to [2,52] stable conditions prevail at Horns Rev around 20% to 25% of the time for westerly flow and around 35% of the time for easterly flow. Thus there is potential

for atmospheric processes of downward mixing of warmer air potentially heating the ocean surface during stable stratification.

Satellite-based SST can be retrieved with an accuracy of 0.1 K while satellite-based LST has a target accuracy of 1 K [53]. The reasons for this difference in accuracy of SST vs. LST are due to the ocean being approximately homogenous and isothermal with relatively low temporal variation and with emissivity near black body, while most land surfaces are heterogeneous and non-isothermal with high temporal variation and with emissivity of grey body. Emissivity on land varies with vegetation cover, surface moisture and viewing angle and generally, an uncertainty of 1% in emissivity will result in about 0.5 K error in the LST [53]. Thus from the perspective of the SST retrieval accuracy it would be feasible to quantify wake-induced warming effects offshore. In fact, only the relative difference within the wake influenced regions versus neighboring non-disturbed regions would need to be compared as in the land-based studies [3,50,51]. However, due to the higher heat capacity of water and the continuous mixing by wind and ocean currents, such downward mixing of warmer air would need to be persistent in order to have a significant effect, and be measurable. At the time of the photos it is overcast, thus an investigation at suitable resolution cannot be performed.

Nonetheless, the case study pictures from Horns Rev and the WRF model results indicate the drying effect within the far wake of an offshore wind farm. These results are novel and indicative of the same atmospheric processes taking place at large land-based wind farm during stable conditions.

The wind farm wake photos from 12 February 2008 tell a much different story about the atmospheric flow and wind farm wake conditions than this new case from 2016. On that day in 2008 warm water advection fog occurred [16,17]. The fog layer was very shallow upwind of the turbines. The cold humid air above warmer sea was re-condensed to fog in the wake by upward mixing of saturated air. The atmospheric stratification was unstable, the turbulence intensity was high and winds were very weak, near the cut in wind speed of ~4 m/s. Most front row wind turbines and a few others were in operation with very low production (~80 kW out of 2000 kW rated power) while the majority of turbines were stopped due to low winds. From visual inspection of the photos from 2008 a bumpy convective appearance of fog is seen with wide wakes. In contrast, the photos from 2016 show fog in narrow wakes with a smooth appearance. The two situations can be characterized from dispersion theory as looping plume pattern in unstable conditions and fanning plume pattern in stable conditions [54] (pp. 322–327).

Some similarities between the two photo cases with fog in wind farms are: (i) a shallow undisturbed fog layer near the sea surface upwind of the turbines; (ii) fog plumes emerging at hub-height due to wind turbine rotation; and (iii) high level clouds that allow just enough sunshine coming through to outline clear sunlit and shaded regions of the curvature of fog downwind of the turbines.

In summary, the wind farm wake case at Horns Rev on 12 February 2008 [17] is highly contrasting to the case on 25 January 2016. The differences are: wind speed near cut in vs. rated speed; few turbines in operation vs. most turbines in operation; unstable vs. stable atmospheric stratification; and cold humid air above a warm sea surface causing warm water advection fog vs. warm humid air above a cold sea surface causing cold water advection fog. Within the near wakes the 2008 case is explained by warm humid air up-drafted from below in the counter-rotating swirl. The condensation appears to take place where high axial velocity and high TKE exist. In contrast, in the 2016 case the fog in the near wake occurs, where the temperature reaches the dew-point, which seems to be homogenously distributed at the lower parts and in the left of the wake. Furthermore, the 2016 case is highly interesting as in the far wake region the photos reveal clearing of the fog further into the farm. This is explained from mixing of warm air from aloft that dispersed the fog. This result is obtained using the WRF model with inclusion of the wind farm and without wind farm, to quantify the drying effect. Key data for the two cases are summarized in Table 1.

Table 1. Wind farm wake conditions at two Horns Rev photo cases.

Information	12 February 2008	25 January 2016
Wind farm name	Horns Rev 1	Horns Rev 2
Number of turbines	80	91
Rated production (kW)	2000	2300
Actual production (kW)	~80	~2300
Wind turbine status	Few turbines at cut-in	Most turbines at rated
Wind speed (m/s)	~4	~13
Wind direction (degrees)	~181	~223
Air temperature (°C)	~3.5	~8.0
Sea surface temperature (°C)	~5.0	~5.2
Turbulence intensity (%)	~17	~3
Atmospheric stability	Unstable	Stable
Wake expansion	Wide, looping	Narrow, fanning
Type of fog upstream	Warm water advection fog	Cold water advection fog
Near wake process	Condensation in high TKE	Saturation dew-point at low height
Far wake process	None	Dispersion due to mixing air aloft

8. Conclusions

The photos of foggy conditions from Horns Rev 2 wind farm on 25 January 2016 show an exceptional case of cold water advection fog and stable conditions. Due to the stable stratification the wakes are long and narrow with a smooth appearance. The wind speed is near rated speed (~13 m/s) thus most turbines produce at rated capacity. The fog in the near wake is caused by upward moving air parcels from the shallow fog layer, and the air reaches the dew point temperature in the lower and left parts of the wind farm wake, thus fog emerges in a cone-shape wake structure downwind of the turbines. The conclusion is based on LES modelling of the wake dynamics, which have been used to elucidate on the fog generation through a simple temperature and phase-transition scheme. Hence, LES results and visually observed fog cones are compared directly for the first time.

The wake photos from Horns Rev 1 wind farm on 12 February 2008 are by all means presenting an opposing situation. The fog is warm water advection fog and the atmosphere is unstable. The wind speed is near the cut in wind speed (~4 m/s) and most turbines are idle and only front row turbines and few others operate with very low production. The wind turbine wakes cause condensation in wake regions with high TKE and the wakes are seen to be broad with a convective appearance.

Finally, the photos from 2016 show clearing of the fog in the far wake. The physical processes involved in this are modelled from WRF without and with a parametrization for the wind farm included, and the difference in liquid water content show that a drying effect appear downwind of the wind farms for more than 100 km. Thus the photos confirm this drying process, which for the first time is visualized and modelled for an offshore wind farm.

Acknowledgments: We warmly acknowledge all data used. The photographs are from Bel Air Aviation Helicopter Service. SCADA data and meteorological observations are from DONG Energy. Satellite SST data are from GHRSST, DMI and MyOcean regional data assembly center. ASCAT data are from KNMI OSI SAF. Radiosonde data is from UWYO and the cloud cover map is from ECMWF.

Author Contributions: N.G.N. analyzed the Horns Rev 2 data, P.J.H.V. ran the WRF model, I.K. performed the satellite analysis, S.J.A. ran the LES model, J.B. analyzed the meteorology and C.B.H. wrote the paper and received input from all co-authors on the text.

Conflicts of Interest: The authors declare no conflict of interest.

Abbreviations

ASCAT	Advanced Scatterometer
DMI	Danish Meteorological Institute
ECMWF	European Centre Medium-range Weather Forecast
ERA-Interim	ECMWF Re-Analysis

EUMETSAT	European Organization for the Exploitation of Meteorological Satellites
EWEA	European Wind Energy Association
EWP	Explicit Wake Parametrisation
GHRSST	Group for High Resolution SST
GWEC	Global Wind Energy Association
KNMI	Royal Netherlands Meteorological Institute
LST	Land surface temperature
LES	Large Eddy Simulation
Lidar	Light detection and ranging
MYNN	Mellor-Yamada-Nakanishi-Niino
N	North
SCADA	Supervisory Control and Data Acquisition system
SEVIRI	Spinning Enhanced Visible and Infrared Imager
SST	Sea surface temperature
SSW	South southwest
SW	Southwest
TKE	turbulent kinetic energy
UTC	Coordinated Universal Time
UTM	Universal Transverse Mercator coordinate system
UWYO	University of Wyoming
W	West
WRF	Weather Research & Forecasting
WSW	West southwest

Appendix A

Table A1. Meteorological observations from the lidar on 25 January 2016 at various heights for the 10-min periods before, at, and after the wake photos. Wind speed (U), wind direction (D), turbulence intensity (TI), and data quality (Q) at height (H).

	12.40 UTC				**12.50 UTC**				**13.00 UTC**			
H	**U**	**D**	**TI**	**Q**	**U**	**D**	**TI**	**Q**	**U**	**D**	**TI**	**Q**
m	**m/s**	°	**%**	**-**	**m/s**	°	**%**	**-**	**m/s**	°	**%**	**-**
65.75	10.54	223.10	8.44	100.00	10.56	223.30	7.95	100.00	10.16	222.90	8.27	100.00
68.75	10.69	223.40	8.61	100.00	10.69	223.80	8.14	100.00	10.26	223.30	8.48	100.00
85.75	11.54	224.90	8.93	100.00	11.39	226.00	8.87	100.00	10.96	225.10	9.49	100.00
105.75	12.59	227.90	8.58	100.00	12.42	227.80	8.45	100.00	11.96	226.60	9.11	100.00
125.75	13.53	230.50	7.83	100.00	13.40	229.90	8.13	100.00	13.08	228.20	8.79	100.00
145.75	14.69	233.20	7.22	99.00	14.65	233.00	7.37	100.00	14.30	230.90	7.69	100.00
185.75	16.65	237.70	9.01	50.00	16.33	237.30	6.06	35.00	16.60	237.50	5.18	84.00
205.75	15.15	242.10	10.30	1.00	17.41	238.40	5.57	3.00	17.51	239.10	6.97	9.00
225.75	N/A	N/A	N/A	0.00	N/A	N/A	N/A	0.00	N/A	N/A	N/A	0.00
245.75	N/A	N/A	N/A	0.00	N/A	N/A	N/A	0.00	N/A	N/A	N/A	0.00

Table A2. Pressure (Pr), temperature (T) and relative humidity (RH) from meteorological station on 25 January 2016 at the top of the transformer station for the 10-min periods before, at, and after the wake photos.

UTC	**Pr (hPa)**	**T (°C)**	**RH (%)**
12:40	1014.8	8.16	100
12:50	1014.81	7.97	100
13:00	1014.88	7.90	100

Table A3. The SCADA data from Horns Rev 2 on 25 January 2016 are listed for each turbine (Tu) for three 10-min periods; before, at and after the wake photos. The table contains data on nacelle wind speed (U), produced power (P), rotational speed (R), yaw direction (D) and quality flag (Q) for the production data with 1 "Measurement valid", 5 "Rotor stopped", 6 "Start or stop sequence", 9 "No data available".

	12.40 UTC					12.50 UTC					13.00 UTC				
Tu	**U**	**P**	**R**	**D**	**Q**	**U**	**P**	**R**	**D**	**Q**	**U**	**P**	**R**	**D**	**Q**
#	**m/s**	**kW**	**RPM**	°	**-**	**m/s**	**kW**	**RPM**	°	**-**	**m/s**	**kW**	**RPM**	°	**-**
A01	11.7	2309	16.0	219.2	1	11.3	2309	16.0	216.5	1	11.9	2311	16.0	219.1	1
A02	12.1	2310	15.9	218.7	1	11.7	2310	15.9	216.2	1	12.2	2310	15.9	219.8	1
A03	11.9	2309	16.0	218.4	1	11.6	2309	16.0	217.5	1	11.8	2309	16.0	219.1	1
A04	12.1	2309	16.0	218.0	1	11.9	2307	16.0	216.5	1	12.0	2308	16.0	218.1	1
A05	11.9	2308	16.0	217.1	1	11.9	2308	16.0	217.1	1	11.8	2308	16.0	217.8	1
A06	12.0	2310	16.0	216.9	1	12.3	2309	16.0	215.9	1	11.9	2308	16.0	217.5	1
A07	11.1	−3	0.0	220.1	5	11.4	−3	0.0	220.1	5	10.7	−3	0.0	220.1	5
B01	12.0	2311	16.0	218.6	1	10.1	2195	15.9	216.5	1	11.5	2309	16.0	218.6	1
B02	12.0	2310	16.0	218.1	1	11.4	2306	16.0	215.8	1	11.7	2310	16.0	217.8	1
B03	12.0	2310	16.0	218.4	1	11.9	2310	16.0	216.8	1	12.0	2311	16.0	218.2	1
B04	11.9	2310	16.0	218.0	1	11.9	2311	16.0	216.1	1	11.9	2311	16.0	217.3	1
B05	12.3	2312	16.0	217.9	1	12.5	2313	16.0	216.3	1	12.1	2312	16.0	217.2	1
B06	12.3	2309	16.0	217.6	1	12.9	2309	16.0	217.2	1	12.2	2309	16.0	218.0	1
B07	12.3	2306	16.0	217.6	1	12.9	2309	16.0	217.1	1	12.2	2308	15.9	217.4	1
C01	10.4	2288	16.0	218.8	1	8.4	1570	15.7	216.9	1	9.5	1843	15.9	218.2	1
C02	11.1	2286	16.0	218.3	1	9.1	1884	15.9	217.5	1	10.4	2149	15.9	218.5	1
C03	12.3	2303	16.0	−141.3	1	10.2	2274	15.9	−143.5	1	11.5	2276	16.0	−142.0	1
C04	12.0	2307	16.0	217.0	1	10.9	2303	16.0	215.7	1	11.3	2308	16.0	216.2	1
C05	11.9	2307	16.0	218.4	1	11.9	2309	16.0	216.2	1	11.7	2307	16.0	216.9	1
C06	11.8	2308	16.0	217.9	1	12.1	2310	16.0	216.3	1	11.9	2311	16.0	217.2	1
C07	12.0	2306	16.0	218.1	1	12.2	2307	16.0	217.2	1	12.2	2307	15.9	218.4	1
D01	8.9	1769	15.9	220.6	1	8.5	1514	15.7	218.9	1	8.0	1436	15.5	217.5	1
D02	9.1	1933	15.9	221.7	1	8.3	1466	15.6	217.8	1	8.0	1447	15.6	218.0	1
D03	9.0	2045	16.0	219.0	1	7.9	1553	15.8	216.8	1	7.9	1530	15.8	216.5	1
D04	9.4	2197	15.9	218.6	1	8.6	1812	15.9	216.0	1	8.4	1837	15.9	218.6	1
D05	10.9	2298	16.0	218.6	1	9.3	2009	16.0	217.4	1	10.2	2207	16.0	218.5	1
D06	11.1	2305	16.0	218.4	1	9.7	2246	16.0	216.4	1	11.0	2268	16.0	218.3	1
D07	11.8	2307	16.0	218.0	1	11.7	2309	16.0	216.8	1	11.8	2308	16.0	219.0	1
E01	9.1	1780	15.8	221.7	1	9.7	1892	15.9	220.7	1	9.5	1774	15.8	220.6	1
E02	9.1	1850	15.9	221.9	1	9.4	1905	15.9	220.8	1	9.2	1783	15.9	219.6	1
E03	9.2	2002	15.9	220.6	1	9.9	2038	16.0	219.2	1	9.6	1919	15.9	217.7	1
E04	9.2	2046	15.9	219.5	1	9.4	1956	15.9	218.8	1	8.7	1755	15.9	217.1	1
E05	9.6	2268	16.0	217.8	1	9.7	2180	15.9	217.3	1	8.8	1886	16.0	218.3	1
E06	10.2	2306	16.0	217.9	1	10.7	2306	16.0	214.9	1	9.2	2144	16.0	217.0	1
E07	11.5	2308	15.9	218.5	1	11.4	2307	16.0	216.1	1	11.7	2308	16.0	218.8	1
F01	10.3	2223	16.0	221.7	1	10.9	2301	16.0	221.1	1	10.5	2256	16.0	220.8	1
F02	10.4	2238	16.0	221.9	1	11.3	2299	16.0	220.9	1	11.2	2306	16.0	220.5	1
F03	10.5	2224	15.9	221.5	1	11.1	2297	16.0	220.0	1	10.9	2291	16.0	220.3	1
F04	10.3	2304	16.0	219.3	1	10.7	2304	16.0	219.8	1	10.4	2293	16.0	221.1	1
F05	11.1	2307	16.0	218.5	1	11.4	2305	16.0	216.7	1	10.9	2290	16.0	217.8	1
F06	12.1	2306	16.0	217.8	1	12.1	2308	16.0	216.8	1	12.2	2307	16.0	218.7	1
F07	12.1	2308	15.9	218.8	1	11.9	2308	16.0	216.9	1	12.0	2308	16.0	218.7	1
G01	10.5	2273	16.0	221.5	1	10.5	2288	16.0	221.3	1	10.4	2270	16.0	218.6	1
G02	10.8	2295	16.0	219.9	1	10.9	2300	16.0	220.0	1	10.8	2290	16.0	219.1	1
G03	11.1	2284	16.0	218.8	1	11.0	2304	16.0	218.5	1	11.7	2305	16.0	218.7	1
G04	11.2	2285	16.0	217.9	1	10.9	2300	16.0	216.7	1	12.0	2307	16.0	218.4	1
G05	11.3	2301	16.0	216.7	1	11.2	2307	16.0	215.6	1	12.2	2310	16.0	218.4	1
G06	11.6	2303	16.0	216.5	1	11.6	2309	16.0	216.3	1	11.6	2309	16.0	218.1	1
G07	12.8	−5	0.6	111.4	6	12.6	−5	0.7	111.4	6	12.8	−6	0.7	111.4	6
H01	10.3	2140	16.0	223.6	1	10.2	2157	16.0	223.1	1	10.4	2205	16.0	224.0	1
H02	10.2	2122	16.0	221.4	1	10.7	2253	16.0	221.8	1	10.7	2237	16.0	222.2	1
H03	10.3	2203	16.0	220.0	1	10.6	2283	15.9	221.5	1	10.4	2241	16.0	222.3	1
H04	10.5	2263	16.0	218.5	1	10.7	2294	16.0	219.6	1	10.5	2274	16.0	219.0	1
H05	10.0	2258	16.0	216.3	1	10.1	2265	16.0	218.0	1	9.9	2245	16.0	217.6	1
H06	11.1	2307	16.0	215.9	1	10.8	2307	16.0	215.4	1	11.8	2311	16.0	217.3	1
H07	N/A	N/A	N/A	N/A	9	N/A	N/A	N/A	N/A	9	N/A	N/A	N/A	N/A	9

Table A3. *Cont.*

	12.40 UTC					12.50 UTC					13.00 UTC				
Tu	**U**	**P**	**R**	**D**	**Q**	**U**	**P**	**R**	**D**	**Q**	**U**	**P**	**R**	**D**	**Q**
#	**m/s**	**kW**	**RPM**	°	**-**	**m/s**	**kW**	**RPM**	°	**-**	**m/s**	**kW**	**RPM**	°	**-**
I01	9.9	1960	15.9	224.1	1	10.1	1992	15.9	223.0	1	9.9	2004	15.9	222.6	1
I02	9.7	1988	16.0	222.0	1	10.2	2138	16.0	222.7	1	10.3	2175	16.0	223.2	1
I03	10.3	2207	16.0	221.2	1	10.5	2230	16.0	222.1	1	10.4	2255	16.0	221.3	1
I04	10.3	2227	16.0	218.7	1	10.6	2279	16.0	220.5	1	10.5	2276	16.0	220.6	1
I05	10.5	2232	16.0	218.0	1	10.7	2305	16.0	219.8	1	10.5	2297	15.9	218.3	1
I06	10.9	2286	16.0	215.0	1	11.4	2310	16.0	217.3	1	11.2	2309	16.0	217.9	1
I07	11.0	2308	16.0	214.4	1	11.4	2308	16.0	217.2	1	11.6	2308	16.0	218.1	1
J01	9.6	1872	16.0	222.9	1	10.2	2082	16.0	224.3	1	10.3	2120	16.0	224.8	1
J02	10.3	2031	15.9	222.4	1	10.8	2266	16.0	224.1	1	10.7	2232	15.9	223.6	1
J03	10.5	2172	16.0	220.6	1	10.8	2295	16.0	222.6	1	10.9	2297	16.0	222.5	1
J04	N/A	N/A	N/A	N/A	9	N/A	N/A	N/A	N/A	9	N/A	N/A	N/A	N/A	9
J05	10.5	2227	16.0	219.0	1	10.8	2305	16.0	221.0	1	10.9	2307	16.0	219.9	1
J06	10.7	2289	16.0	215.6	1	11.6	2309	16.0	218.1	1	11.6	2308	16.0	218.0	1
J07	10.4	2274	15.9	214.6	1	11.4	2312	15.9	216.6	1	11.3	2309	15.9	216.8	1
K01	9.7	1952	15.9	221.9	1	10.5	2219	15.9	224.9	1	10.4	2153	15.9	223.5	1
K02	10.6	2048	15.9	221.6	1	11.2	2281	16.0	224.7	1	11.1	2278	16.0	223.1	1
K03	10.3	2171	16.0	221.1	1	10.7	2306	16.0	224.1	1	10.9	2306	16.0	221.4	1
K04	10.6	2274	16.0	219.4	1	10.9	2306	16.0	222.7	1	11.2	2305	16.0	220.8	1
K05	10.8	2297	16.0	218.6	1	11.0	2307	16.0	219.2	1	10.9	2305	16.0	218.4	1
K06	10.6	2261	16.0	216.9	1	10.9	2307	16.0	219.2	1	10.9	2305	16.0	218.2	1
K07	10.3	2197	15.9	213.1	1	11.9	2309	16.0	216.6	1	11.9	2309	16.0	216.2	1
L01	9.5	1826	15.8	221.7	1	10.2	2099	15.9	225.0	1	10.4	2157	15.9	224.0	1
L02	9.8	1963	16.0	220.9	1	10.6	2242	16.1	224.5	1	10.9	2267	16.1	224.2	1
L03	10.8	−3	0.0	30.1	5	11.7	−3	0.0	30.1	5	12.2	−3	0.0	30.1	5
L04	10.2	2141	15.9	220.0	1	10.8	2301	16.0	221.2	1	11.2	2305	16.0	220.6	1
L05	10.6	2288	16.0	219.0	1	11.0	2308	16.0	220.1	1	11.6	2307	16.0	218.8	1
L06	10.5	2251	16.0	218.8	1	11.0	2307	16.0	218.8	1	11.3	2305	16.0	217.5	1
L07	10.1	2151	15.9	215.0	1	11.1	2308	16.0	215.1	1	11.2	2300	16.0	214.1	1
M01	8.1	1455	15.2	220.9	1	9.8	2031	15.9	223.7	1	9.8	2027	15.9	223.9	1
M02	8.8	1623	15.5	220.0	1	10.1	2097	15.9	223.3	1	10.1	2069	15.9	221.6	1
M03	9.7	1896	15.9	218.8	1	10.3	2152	16.0	220.6	1	10.4	2241	16.0	220.8	1
M04	9.4	1827	15.8	217.9	1	10.5	2258	15.9	222.0	1	10.9	2261	16.0	221.5	1
M05	10.2	2104	15.9	220.5	1	11.1	2290	16.0	221.7	1	11.4	2300	16.0	220.7	1
M06	10.1	2139	15.9	219.5	1	10.0	2183	15.9	220.1	1	10.2	2136	15.9	220.7	1
M07	9.8	2138	16.0	217.0	1	10.1	2262	16.0	218.4	1	9.3	2153	15.9	218.0	1

References

1. Barthelmie, R.J.; Pryor, S.C.; Frandsen, S.; Hansen, K.; Schepers, G.; Rados, K.; Schlez, W.; Neubert, A.; Jensen, L.E.; Neckelmann, S. Quantifying the impact of wind turbine wakes on power output at offshore wind farms. *J. Atmos. Ocean. Technol.* **2010**, *27*, 1302–1317. [CrossRef]
2. Hansen, K.; Barthelmie, R.J.; Jensen, L.E.; Sommer, A. The impact of turbulence intensity and atmospheric stability on power deficits due to wind turbine wakes at Horns Rev wind farm. *Wind Energy* **2012**, *15*, 183–196. [CrossRef]
3. Smith, C.M.; Barthelmie, R.J.; Pryor, S.C. In situ observations of the influence of a large onshore wind farm on near-surface temperature, turbulence intensity and wind speed profiles. *Environ. Res. Lett.* **2013**, *8*, 034006. [CrossRef]
4. Eriksson, O.; Mikkelsen, R.; Hansen, K.S.; Nilsson, K.; Ivanell, S. Analysis of long distance wakes of Horns Rev I using actuator disc approach. *J. Phys. Conf. Ser.* **2014**, *555*, 012032. [CrossRef]
5. Gaumond, M.; Réthoré, P.-E.; Ott, S.; Peña, A.; Bechmann, A.; Hansen, K.S. Evaluation of the wind direction uncertainty and its impact on wake modeling at the Horns Rev offshore wind farm. *Wind Energy* **2014**, *17*, 1169–1178. [CrossRef]
6. Nygaard, N.G. Wakes in very large wind farms and the effect of neighbouring wind farms. In Proceedings of the TORQUE2014: 5. Science of Making Torque from Wind Conference, Copenhagen, Denmark, 18–20 June 2014.

7. Jimenez, P.A.; Navarro, J.; Palomares, A.M.; Dudhia, J. Mesoscale modeling of offshore wind turbine wakes at the wind farm resolving scale: A composite-based analysis with the Weather Research and Forecasting model over Horns Rev. *Wind Energy* **2015**, *18*, 559–566. [CrossRef]
8. Wu, Y.T.; Porté-Agel, F. Modeling turbine wakes and power losses within a wind farm using LES: An application to the Horns Rev offshore wind farm. *Renew. Energy* **2015**, *75*, 945–955. [CrossRef]
9. Nygaard, N.G.; Hansen, S.D. Wake effects between two neighbouring wind farms. *J. Phys. Conf. Ser.* **2016**, *753*, 032020. [CrossRef]
10. Iungo, G.V.; Porté-Agel, F. Volumetric scans of wind turbine wakes performed with three simultaneous wind LiDARs under different atmospheric stability regimes. *J. Phys. Conf. Ser.* **2014**, *524*, 012164. [CrossRef]
11. Wang, H.; Barthelmie, R.J. Wind turbine wake detection with a single Doppler wind lidar. *J. Phys. Conf. Ser.* **2015**, *625*, 012017. [CrossRef]
12. Vollmer, L.; van Dooren, M.; Trabucchi, D.; Schneemann, J.; Steinfeld, G.; Witha, B.; Trujillo, J.; Kühn, M. First comparison of LES of an offshore wind turbine wake with dual-Doppler lidar measurements in a German offshore wind farm. *J. Phys. Conf. Ser.* **2015**, *625*, 012001. [CrossRef]
13. Hirth, B.D.; Schroeder, J.L.; Scott Gunter, W.; Guynes, J.G. Measuring a Utility-Scale Turbine Wake Using the TTUKa Mobile Research Radars. *J. Atmos. Ocean. Technol.* **2012**, *29*, 765–771. [CrossRef]
14. Christiansen, M.B.; Hasager, C.B. Using airborne and satellite SAR for wake mapping offshore. *Wind Energy* **2006**, *9*, 437–455. [CrossRef]
15. Hasager, C.B.; Vincent, P.; Badger, J.; Badger, M.; di Bella, A.; Pena Diaz, A.; Volker, P. Using Satellite SAR to Characterize the Wind Flow around Offshore Wind Farms. *Energies* **2015**, *8*, 5413–5439. [CrossRef]
16. Emeis, S. Meteorological explanation of wake clouds at Horns Rev wind farm. *DEWI Mag.* **2010**, *37*, 52–55.
17. Hasager, C.B.; Rasmussen, L.; Peña, A.; Jensen, L.E.; Réthoré, P.-E. Wind Farm Wake: The Horns Rev Photo Case. *Energies* **2013**, *6*, 696–716. [CrossRef]
18. Bhaganagar, K.; Debnath, M. Implications of Stably Stratified Atmospheric Boundary Layer Turbulence on the Near-Wake Structure of Wind Turbines. *Energies* **2014**, *7*, 5740–5763. [CrossRef]
19. Hancock, P.E.; Pascheke, F. Wind-tunnel simulations of the wakes of large wind turbines: Part 2, the wake flow. *Bound.-Layer Meteorol.* **2014**, *151*, 23–37. [CrossRef]
20. Hancock, P.E.; Zhang, S.; Pascheke, F.; Hayden, P. Wind tunnel simulation of a wind turbine wake in neutral, stable and unstable wind flow. *J. Phys. Conf. Ser.* **2014**, *555*, 01204. [CrossRef]
21. Chamorro, L.P.; Porté-Agel, F. Effects of thermal stability and incoming boundary-layer flow characteristics on wind-turbine wakes: A wind-tunnel study. *Bound.-Layer Meteorol.* **2010**, *136*, 515–533. [CrossRef]
22. Hancock, P.E.; Zhang, S. A Wind-Tunnel Simulation of the Wake of a Large Wind Turbine in a Weakly Unstable Boundary Layer. *Bound.-Layer Meteorol.* **2015**, *156*, 395–413. [CrossRef]
23. EWEA. European Wind Energy Association: The European Offshore Wind Industry—Key Trends and Statistics 2015. 2016. Available online: http://www.ewea.org/fileadmin/files/library/publications/statistics/EWEA-European-Offshore-Statistics-2015.pdf (accessed on 1 March 2017).
24. Global Wind Energy Council. Available online: http://www.gwec.net/global-figures/market-forecast-2012-2016/ (accessed on 1 March 2017).
25. Courtney, M.; Wagner, R.; Lindelöw, P. Testing and comparison of lidars for profile and turbulence measurements in wind energy. *IOP Conf. Ser. Earth Environ. Sci.* **2008**, *1*, 012021. [CrossRef]
26. Gottschall, J.; Courtney, M.S.; Wagner, R.; Jørgensen, H.E.; Antoniou, I. Lidar profilers in the context of wind energy—A verification procedure for traceable measurements. *Wind Energy* **2012**, *15*, 147–159. [CrossRef]
27. Sathe, A.; Mann, J.; Gottschall, J.; Courtney, M. Can Wind Lidars Measure Turbulence? *J. Atmos. Ocean. Technol.* **2011**, *28*, 853–868. [CrossRef]
28. Ocean and Sea Ice Satellite Application Facility. Available online: http://www.osi-saf.org (accessed on 1 March 2017).
29. Høyer, J.L.; She, J. Optimal interpolation of sea surface temperature for the North Sea and Baltic Sea. *J. Mar. Syst.* **2007**, *65*, 176–189. [CrossRef]
30. Høyer, J.L.; Karagali, I. Sea surface temperature climate data record for the North Sea and Baltic Sea. *J. Clim.* **2016**, *29*, 2529–2541. [CrossRef]
31. Karagali, I.; Høyer, J.L. Observations and modelling of the diurnal SST cycle in the North and Baltic Seas. *J. Geophys. Res. Oceans* **2013**, *118*, 4488–4503. [CrossRef]

32. Karagali, I.; Høyer, J.L. Characterisation and quantification of regional diurnal cycles from SEVIRI. *Ocean Sci.* **2014**, *10*, 745–758. [CrossRef]
33. Kátic, I.; Højstrup, J.; Jensen, N.O. A Simple Model for Cluster Efficiency. In Proceedings of the European Wind Energy Association Conference and Exhibition, Rome, Italy, 7–9 October 1986.
34. European Organization for the Exploitation of Meteorological Satellites. Available online: http://en.sat24.com/en (accessed on 1 March 2017).
35. European Centre Medium-Range Weather Forecast. Available online: http://www.ecmwf.int/ (accessed on 1 March 2017).
36. University of Wyoming. Available online: http://weather.uwyo.edu/upperair/sounding.html (accessed on 1 March 2017).
37. Peña, A.; Hahmann, A.N. Atmospheric stability and turbulence fluxes at Horns Rev—An intercomparison of sonic, bulk and WRF model data. *Wind Energy* **2012**, *15*, 717–731. [CrossRef]
38. Skamarock, W.C.; Klemp, J.B.; Dudhia, J.; Gill, D.O.; Barker, D.M.; Duda, M.G.; Huang, X.-Y.; Wang, W.; Powers, J.G. *A Description of the Advanced Research WRF Version 3*; NCAR Technical Note NCAR/TN-475+STR; National Center for Atmospheric Research: Boulder, CO, USA, 2008.
39. Dee, D.P.; Uppala, S.M.; Simmons, A.J.; Berrisford, P.; Poli, P.; Kobayashi, S.; Andrae, U.; Balmaseda, M.A.; Balsamo, G.; Bauer, P.; et al. The ERA-Interim reanalysis: Configuration and performance of the data assimilation system. *Q. J. R. Meteorol. Soc.* **2011**, *137*, 553–597. [CrossRef]
40. Monin, A.S.; Obukhov, A.M. Basic laws of turbulent mixing in the surface layer of the atmosphere. *Tr. Akad. Nauk. SSSR Geophiz. Inst.* **1954**, *24*, 163–187.
41. Nakanishi, M.; Niino, H. Development of an improved turbulence closure model for the atmospheric boundary layer. *J. Meteorol. Soc. Jpn.* **2009**, *87*, 895–912. [CrossRef]
42. Volker, P.H.J.; Badger, J.; Hahmann, A.N.; Ott, S. The Explicit Wake Parametrisation V1.0: A wind farm parametrisation in the mesoscale model WRF. *Geosci. Model Dev.* **2015**, *8*, 3715–3731. [CrossRef]
43. Sørensen, N.N. General Purpose Flow Solver Applied to Flow over Hills. Ph.D. Thesis, Technical University of Denmark, Kongens Lyngby, Denmark, 1995.
44. Michelsen, J.A. Basis3D—A Platform for Development of Multiblock PDE Solvers. Ph.D. Thesis, Technical University of Denmark, Kongens Lyngby, Denmark, 1992.
45. Mann, J. The spatial structure of neutral atmospheric surface-layer turbulence. *J. Fluid Mech.* **1994**, *273*, 141–168. [CrossRef]
46. Sørensen, J.N.; Mikkelsen, R.F.; Henningson, D.S.; Ivanell, S.; Sarmast, S.; Andersen, S.J. Simulation of wind turbine wakes using the actuator line technique. *R. Soc. Lond. Philos. Trans. A Math. Phys. Eng. Sci.* **2015**, *373*, 20140071. [CrossRef] [PubMed]
47. Duynkerke, P. Turbulence, radiation and fog in Dutch stable boundary layers. *Bound.-Layer Meteorol.* **1998**, *90*, 447–477. [CrossRef]
48. Van Ulden, A.P.; Holtslag, A.A.M. Estimation of atmospheric boundary layer parameters for diffusion applications. *J. Clim. Appl. Climatol.* **1985**, *24*, 1196–1207. [CrossRef]
49. Peña, A.; Gryning, S.-E.; Hasager, C.B. Comparing mixing-length models of the diabatic wind profile over homogeneous terrain. *Theor. Appl. Climatol.* **2010**, *100*, 325–335. [CrossRef]
50. Baidya Roy, S.; Traiteur, J.J. Impacts of wind farms on surface air temperatures. *Proc. Natl. Acad. Sci. USA* **2010**, *107*, 17899–17904. [CrossRef] [PubMed]
51. Chang, R.; Zhu, R.; Guo, P. A Case Study of Land-Surface-Temperature Impact from Large-Scale Deployment of Wind Farms in China from Guazhou. *Remote Sens.* **2016**, *8*, 790. [CrossRef]
52. Sathe, A.; Gryning, S.-E.; Peña, A. Comparison of the atmospheric stability and wind profiles at two wind farm sites over a long marine fetch in the North Sea. *Wind Energy* **2011**, *14*, 767–780. [CrossRef]
53. Li, Z.-L.; Tang, B.-H.; Wu, H.; Ren, H.; Yan, G.; Wan, Z.; Trigo, I.F.; Sobrino, J.A. Satellite-derived land surface temperature: Current status and perspectives. *Remote Sens. Environ.* **2013**, *131*, 14–37. [CrossRef]
54. Oke, T.R. *Boundary Layer Climates*, 2nd ed.; Methuen: London, UK; New York, NY, USA, 1987.